Available online at www.CivileJournal.org

Civil Engineering Journal

(E-ISSN: 2476-3055; ISSN: 2676-6957)

Vol. 12, No. 03, March, 2026

A Comparative Study on Cyclic Behavior of S-Shaped and U-Shaped Steel Plate Dampers

Zhipeng Zhai [1, 2], Qi Shu [1], Kaiying Yao [1], Yao Hu [3*], Linfa Wang [4]

[1] *Earthquake Engineering Research & Test Center (EERTC), Guangzhou University, Guangzhou 510006, China.*

[2] *Guangdong Provincial Key Laboratory of Earthquake Engineering and Applied Technology, Guangzhou 510006, China.*

[3] *School of Civil Engineering, Central South University, Changsha 410075, China.*

[4] *China Electronic System Construction Engineering Co., Ltd., China.*

Received 07 January 2026; Revised 24 February 2026; Accepted 27 February 2026; Published 01 March 2026

Abstract

The widely used U-shaped steel plate damper (USPD), featured by large deformation capacity and excellent energy dissipation efficiency, is incapable of achieving multi-level seismic control due to single-stage energy dissipation. To tackle this issue, a new S-shaped steel plate damper (SSPD) derived from USPD and sharing identical geometric dimensions is presented, which exploits a bending-tensile yield mechanism to form double-stage energy dissipation behavior. This paper carries out comprehensive numerical investigations with the aim of comparing the cyclic behavior of USPD and SSPD. Firstly, their configuration and working principle are elaborated, and an experimentally validated numerical modeling approach is proposed. Subsequently, numerical parametric analyses are conducted on models with various geometric dimensions. The performance of USPD and SSPD under cyclic loading is evaluated in terms of hysteresis characteristics, damage development, stiffness degradation, energy dissipation, and residual displacement, as well as their performances under low-cycle fatigue loading, which are analyzed. Finally, the calculation formulas for critical mechanical parameters of the dampers are recommended to facilitate the design in engineering practice. The results show that the ability of multi-level seismic control and superior cyclic performance support the application of SSPD in scenarios requiring the demand of multi-level seismic control and dual function of loading-bearing and energy-dissipating.

Keywords: USPD; SSPD; Multi-Level Seismic Control; Hysteretic Performance; Low-Cycle Fatigue.

1. Introduction

The concept of seismic resilience emphasizes structures remaining low-damage and swift recovery after suffering strong earthquakes, which leads to increasing investigations on enhancing the seismic performance of traditional structures that are susceptible to being damaged and challenging to be repaired due to the plastic energy dissipation of structural components [1-3]. In the recent decade, replaceable fuses decoupled from vertically resisting systems and with favorable energy dissipation capacity have been developed for improving structural seismic resilience, such as friction dampers, metallic dampers, viscous dampers, and viscoelastic dampers. Among them, metallic dampers attract extensive research attention and are widely utilized in building engineering, bridge engineering, and ocean engineering due to the advantages of low cost, stable hysteresis loops, high energy efficiency, and insensitivity to temperature and frequency [4-6]. It supplements additional stiffness and dissipates most of the seismic energy to mitigate structural dynamic response and prevent the main structure from severe damage, while it can be quickly replaced post-earthquakes, enabling it to be an economical and efficient technology for improving seismic resilience.

* Corresponding author: yaohuu@csu.edu.cn

https://doi.org/10.28991/CEJ-2026-012-03-01

Many efforts have been conducted in previous studies to innovate various types of metallic dampers, which can be mainly divided into three categories according to the deformation mechanism, including axial-yield type, shear-yield type, and flexural-yield type [7, 8]. The axial-yield type is characterized by a large supplement of stiffness and load resistance, while the flexural-yield type exhibits high energy dissipation efficiency and low forces transmitted to the connecting joint. A kind of flexural-yield damper with large deformation capacity and excellent fatigue performance is widely preferred and applied to various types of structures [5, 9-11], named as a U-shaped steel plate damper (USPD). Ebadi Jamkhaneh et al. [12] conducted a series of static cyclic tests to examine the hysteretic behavior of USPD and installed the dampers into a steel moment-resisting frame for seismic performance upgrading. Taiyari et al. [13] proposed a bracing system composed of U-shaped steel strips. Experimental results verified its high dissipating capacity and large inelastic deformation, and finite element models were established to analyze the effects of dimensional parameters.

Qu et al. [14] similarly developed an energy dissipation brace that consisted of several replaceable U-shaped steel plates. The test results showed that specimens continued to dissipate significant amounts of hysteretic energy even after the formation of the visible ruptures, and the brace, after replacing the damaged steel plates, remained satisfactory in a subsequent earthquake. Furthermore, they adopted stack-thin U-shaped steel plates to substitute the above plates for improving the damper's fatigue performance [15], and the effectiveness was verified through experimental investigations. Oh et al. [16] introduced USPD to enhance the seismic performance of base-isolated frames, and shaking table tests were performed. It pointed out that the dampers can be used as energy-dissipating devices for base isolating systems because they can sustain large displacements without strength and stiffness degradation. Hui et al. [17] employed USDP to mitigate seismic responses of continuous girder bridges under near-fault earthquake excitations; the results validated the effectiveness with a seismic reduction rate of 20~70% in the longitudinal direction of the bridges. Additionally, a sliding USPD with a multi-directional displacement function was invented for avoiding unexpected out-of-plane torsional deformation [18, 19], and a superelastic shape memory alloy USPD was proposed for achieving a self-centering function [20, 21]. Despite the proven effectiveness and widespread application of USPDs, their design philosophy is inherently single-phased. That is, they are typically calibrated to yield at a specific seismic intensity level (e.g., service level earthquake (SLE)), after which their stiffness contribution diminishes. While this is effective for a targeted hazard level, it may not be optimal for structures requiring resilient performance across a spectrum of seismic events, from frequent minor tremors to rare mega-earthquakes.

To address this limitation, hybrid dampers with double yielding stages have been developed nowadays to strive for higher economic efficiency and vibration control of multiple seismic levels. Zhai et al. [22], Dai et al. [23], and Yang et al. [24] proposed a hybrid buckling-restrained brace (BRB) by integrating a friction damper and a BRB. Wen et al. [25] and Eghlimi et al. [26] proposed an asynchronous parallel double-stage BRB and a two-level yielding deformation-controlled ring damper, respectively, via installing damper elements with different yielding displacements in parallel. Their inventions successfully controlled the structural dynamic responses at three levels of SLE, design basis earthquake (DBE), and maximum considered earthquake (MCE). The same methodology was also adopted to improve USPD. For instance, Chen et al. [27] and Cheraghi et al. [28] combined multiple USPD elements with different strengths and stiffnesses to get a multiphase yielding mechanism. However, it should be noted that the above technologies undoubtedly exist shortcomings, such as intricate connection details and potentially lower material utilization efficiency, which could offset their performance benefits in terms of cost-effectiveness and ease of construction. Therefore, a research gap exists in developing a damper that can achieve multi-stage or enhanced performance without compromising the simplicity, geometric uniformity, and high material efficiency inherent to the classic USPD design.

Bridging this gap, Zhai et al. [29] recently proposed a novel S-shaped steel plate damper (SSPD). Critically, the SSPD maintains identical overall dimensions and connection details as the USPD, ensuring practical familiarity and ease of replacement. The fundamental innovation lies in its geometric reconfiguration from a U-shape to an S-shape. This morphological shift transforms the primary deformation mechanism from pure flexure (in USPD) to a combined flexural-tensile action (in SSPD), which is hypothesized to unlock a dual-phase yielding behavior and potentially superior hysteretic properties while preserving geometric compatibility. Given this geometric kinship but fundamental mechanistic difference, a direct and systematic comparison of their seismic performance is not only logical but essential. However, such a comprehensive comparative study is currently absent from the literature. Without it, the practical implications and potential advantages of adopting SSPD over the well-established USPD remain unclear, hindering its informed application in engineering practice.

In response to this gap, the primary objective of this paper is to conduct a comprehensive numerical investigation to elucidate and contrast the cyclic performance of the proposed SSPD against the conventional USPD. To this end, the intrinsic relevance between them is introduced through describing their details and working principles. And high-fidelity finite element models using solid elements are developed and rigorously validated against available experimental data. Subsequently, a suite of parametric numerical analyses is performed to critically compare key performance indicators, including hysteretic characteristics, stiffness degradation patterns, energy dissipation capacity, residual displacement,

and low-cycle fatigue performance. Based on the insights derived from these comparative analyses, practical design equations for predicting the key mechanical properties of both dampers will be formulated through regression analysis, providing valuable tools for engineers. Figure 1 shows the methodology process of this study.

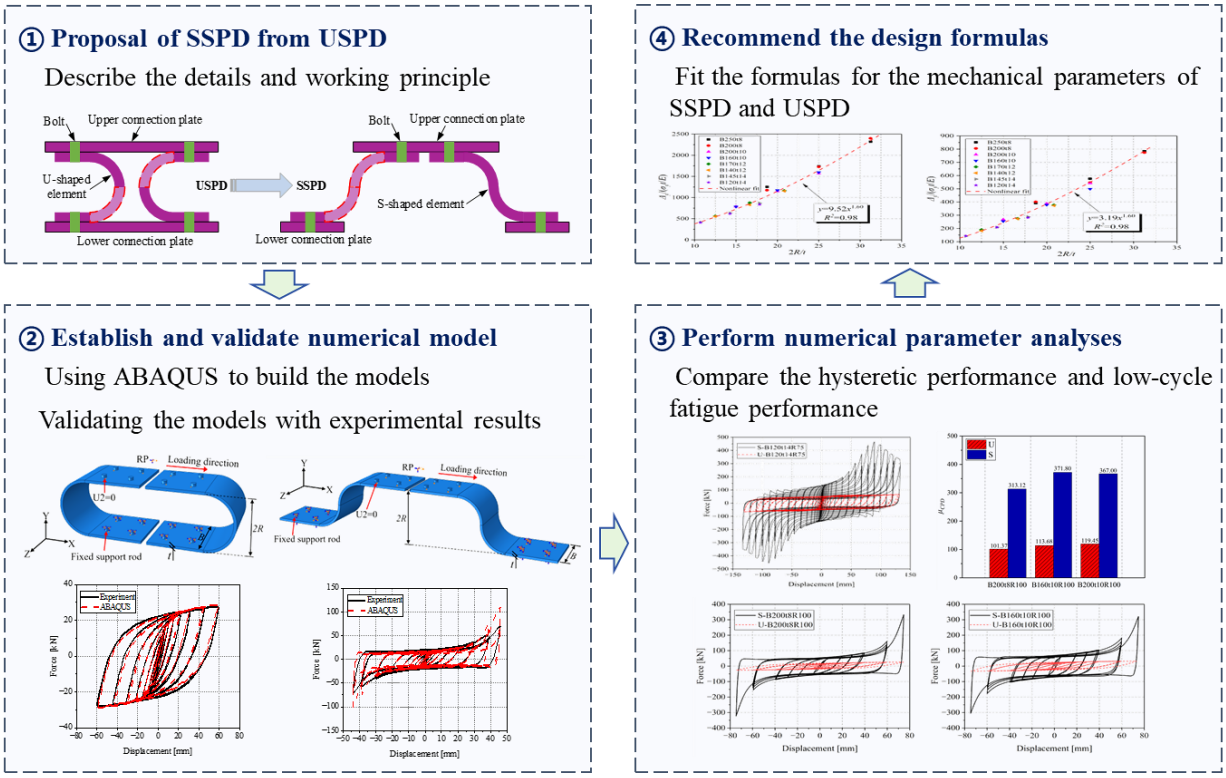

Figure 1. Flowchart of the methodology process

2. Description of USPD and SSPD

USPD generally consists of two U-shaped elements that are bolted to the upper and lower connection plates, as shown in Figure 2. The U-shaped element is fabricated using a mild steel plate through a cold-forming process, which can be divided into the semi-circular arc segment and the ending straight segment. If the lower quarter-circular arc of one U-shaped element is combined with the upper quarter-circular arc of the other, an S-shaped element will be generated, as remarked by the red dashed region in Figure 2. The fabrication of the S-shaped element is the same as that of the U-shaped element, as well as the geometric dimensions. Both of them have the advantages of low cost, convenient installation, and easy replacement post-earthquake.

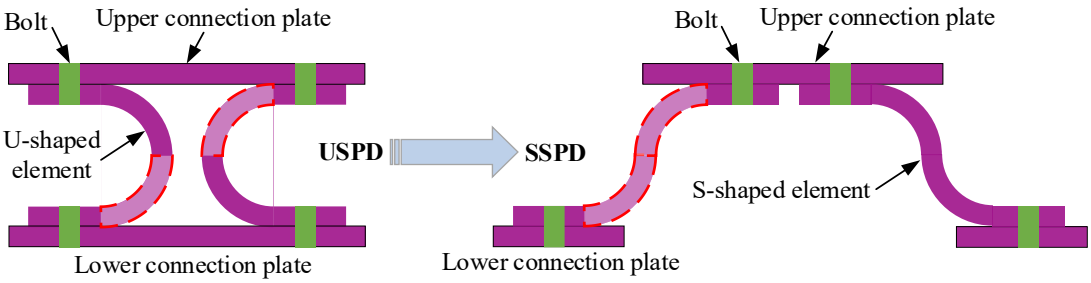

Figure 2. Schematic configuration of USPD and SSPD

Under the action of lateral loads, USPD deforms dominantly by the bending mechanism, and the energy is dissipated through flexural plastic deformation, as indicated in Figure 3(a). The curvature of the semi-circular arc segment is almost constant, maintained as the reciprocal of the radius. For SSPD, bending deformation is generated when the external load is relatively small, and it transitions to tensile deformation as the load increases to a large value, as illustrated in Figure 3(b). Due to the behavior of geometric nonlinearity, the energy dissipation of SSPD is dominated by flexural plasticity at small deformations and by axial plasticity at large deformations, which produces the characteristic of a double yielding stage for SSPD. Meanwhile, the mechanical behavior of axial tension increases the damper's stiffness and strength, which is conducive to controlling structural dynamic responses.

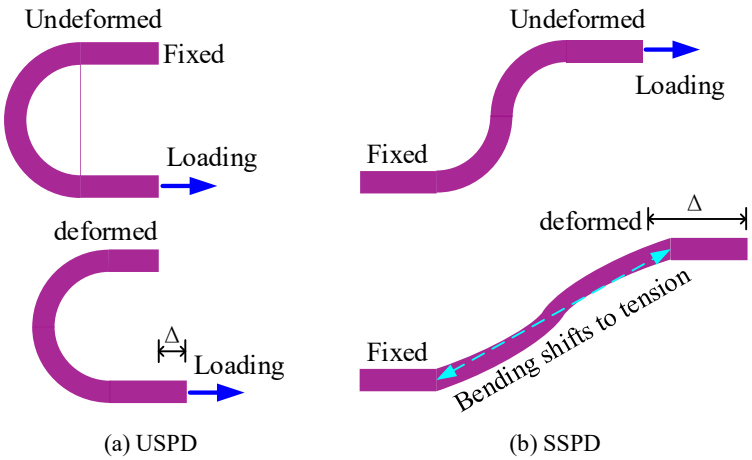

(a) USPD (b) SSPD

Figure 3. Deformation mode of USPD and SSPD

The theoretical formulas for initial stiffness and yielding strength of USPD have been derived in a previous study on the assumption of a fixed boundary, as expressed by Chong et al. [11]:

$$k_{e,U} = \frac{32EB}{27\pi}\left(\frac{t}{2R}\right)^3 \quad (1)$$

$$F_{y,U} = \frac{\sigma_y B t^2}{3R} \quad (2)$$

where, $k_{e,U}$ and $F_{y,U}$ are respectively the initial stiffness and yielding strength; E and σ_y are respectively the Young's modulus and yielding strength of steel material; R is the radius of centerline of the circular arc segment; B and t are the width and thickness of the steel plate, respectively. According to the experimental results, the peak strength $F_{p,U}$ of USPD can be estimated by Equation 3, where λ is the adjustment factor, generally adopted as 1.1~1.3. Note that the formulas are for a damper with two U-shaped elements (see Figure 2).

$$F_{p,U} = \lambda F_{y,U} \quad (3)$$

Similarly, the authors have derived the theoretical formulas of SSPD, as given by Zhai et al. [29]:

$$k_{e,S} = 8EB\left(\frac{t}{2R}\right)^3 \quad (4)$$

$$F_{y,S} = \frac{1.24\sigma_y B t^2}{R} \quad (5)$$

$$F_{p,S} = \sigma_y B t \quad (6)$$

where $k_{e,S}$, $F_{y,S}$ and $F_{P,S}$ are respectively the initial stiffness, yielding strength and peak strength. By these formulas, the values for $k_{e,S}/k_{e,U}$, $F_{y,S}/F_{y,U}$, and $F_{P,S}/F_{p,U}$ can be calculated as 21.2, 3.72 and $3R/\lambda t$, respectively, showing much higher stiffness and strength of SSPD. It should be noted that these formulas are derived from ideal boundary conditions, and the ratios of the mechanical parameters may differ from those above in an actual scenario.

3. Numerical Modelling and Validation

3.1. Numerical Modelling

Numerical models for USPD and SSPD are established by the ABAQUS program, and the same modeling approach as depicted in Figure 4 is adopted for them. The steel plates and bolt rods are modeled utilizing 3D-stress 8-node nonlinear solid elements (C3D8R). To build the interactions between the contact surface of bolt holes and rods, surface-to-surface contacts that possess the normal property of "hard contact" and "penalty" tangential behavior with a friction coefficient of 0.1 are assigned. To better simulate the actual boundary conditions, the end surfaces of bolt holes in the straight segment are restrained in the degree of freedom (DOF) U2 (Y direction). All DOFs of the end surfaces on lower support rods are restrained, and the DOFs of the upper rods are coupled to a reference point (RP) to which the lateral displacement loads are applied. During the analysis, both material and geometric nonlinearities are taken into account. The nonlinear behavior of steel material for U- and S-shaped elements is simulated employing the combined hardening law considering kinematic and isotropic cyclic hardening. Here a combined model with four back-stress coefficient pairs is adopted, as tabulated in Table 1. But the nonlinearity of bolt rods is ignored here due to their elastic behavior, and the elastic material with a Young's Modulus of 210 GPa and Poisson ratio of 0.3 is utilized. It should note that the bolt pretension and possible slip could influence the initial stiffness and early hysteretic response of the dampers. However,

in the current study, these effects were not explicitly discussed due to the following reasons: (a) the focus of the research was primarily on the dampers' behavior under cyclic loading, where the influence of bolt pretension and slip was deemed minor compared to other dominant factors (e.g., material nonlinearity, geometric effects); (b) Including these effects would significantly complicate the model without guaranteed improvements in predictive accuracy for the intended application. From the experimental phenomena and simulation results, these simplifications are reasonable. Additionally, the assumed friction coefficient of 0.1 was based on conservative engineering estimates and a literature review of similar bolted joint configurations. Sensitivity analysis was conducted to evaluate the impact of varying friction coefficients on the models' response. Results showed that the initial stiffness and hysteretic behavior were relatively insensitive to small changes in friction coefficient within the range of 0.0 ~ 0.3.

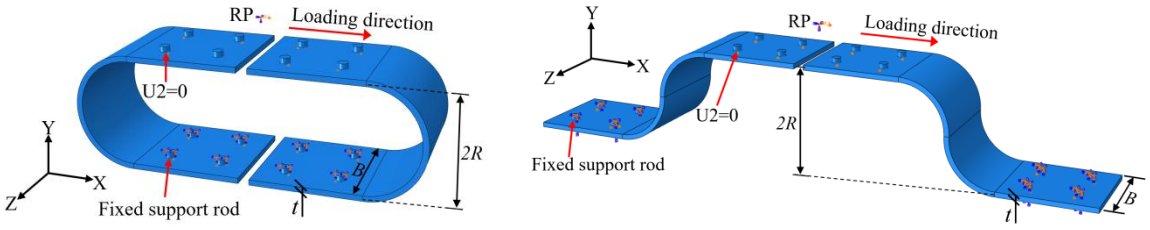

(a) USPD (b) SSPD

Figure 4. Modelling approach

Table 1. The combined hardening parameters

C_1 (MPa)	γ_1	C_2 (MPa)	γ_2	C_3 (MPa)	γ_3	C_4 (MPa)	γ_4
22000	300	1600	120	6000	250	600	30

3.2. Experimental Validation

Several test specimens for USPD and SSPD in previous studies [11, 29] are selected to validate the modeling approach. The dimensions of the three USPD specimens are R=66/75/125 mm, B=70/200/200 mm, and t=12/8/10 mm, and for the three SSPD specimens, they are R=51/64/64 mm, B=40/40/40 mm, and t=6/5/6 mm. By applying the test loading history, the hysteretic curves of the models can be obtained and compared with those of the experiments, as plotted in Figure 5. As can be seen, the numerical curves are in good agreement with the test curves overall. At the last level loading cycle of SSPD, the peak force of the model is obviously larger than the test results, the reasons for which are mainly attributed to: (1) significant thermal residual stresses on the specimen's end plates caused by the cut of the grinding wheel are not considered in the model; (2) the capacity limitation of the loading actuator is attained, causing the peak force of the final level loading to be underestimated.

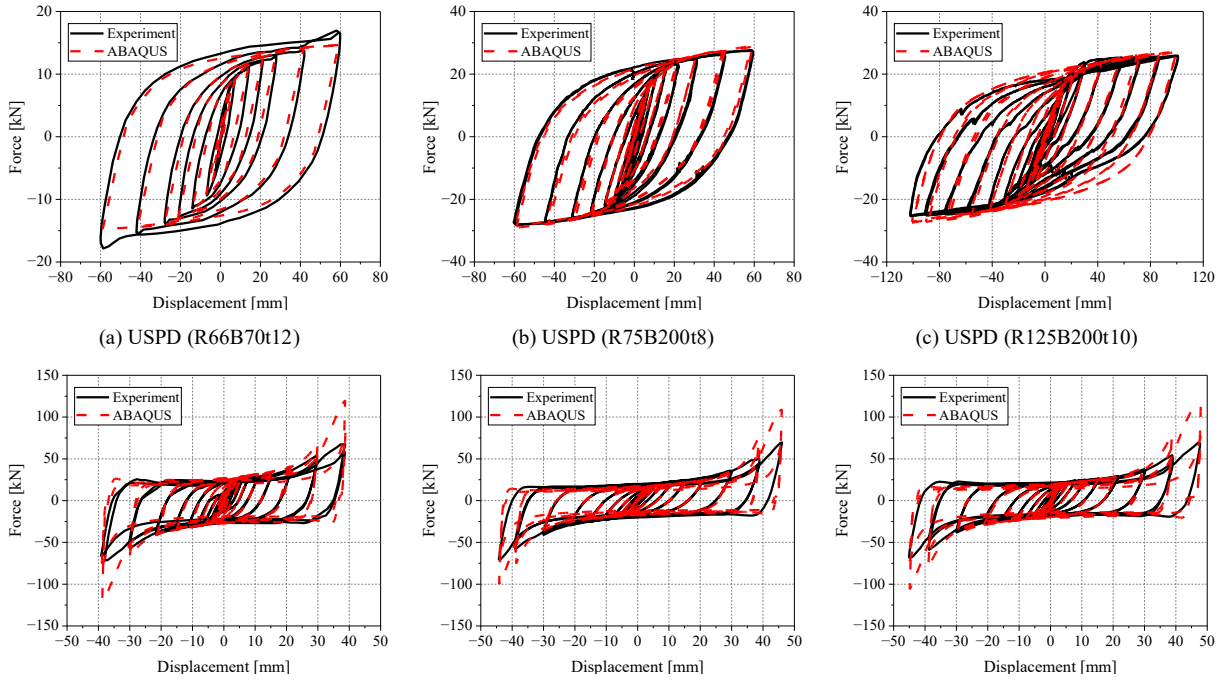

(a) USPD (R66B70t12) (b) USPD (R75B200t8) (c) USPD (R125B200t10)

(d) SSPD (R51B40t6) (e) SSPD (R64B40t5) (f) SSPD (R64B40t6)

Figure 5. Hysteretic curve of numerical models and test specimens

Figure 6 compares the plasticity distribution between the numerical models and test specimens. It can be inferred from the contour plot of Mises stress and equivalent plastic strain (PEEQ) that the damage of the USPD model mainly concentrates at the transition zone between the semi-circular and straight segments, which is consistent with the distribution of cracks observed in the specimen. And it displays a crawler-type rolling deformation mode similar to Figure 2(a). The damage of the SSPD model primarily locates at the middle part of the quarter-circular segment and the section of the bolt hole, which is in accordance with the test observations. Meanwhile, both the model and the specimen show a tension and extrusion-dominated deformation mode. Note that the damage of the hole section can be alleviated by controlling the bolt opening-caused area reduction of the end plate.

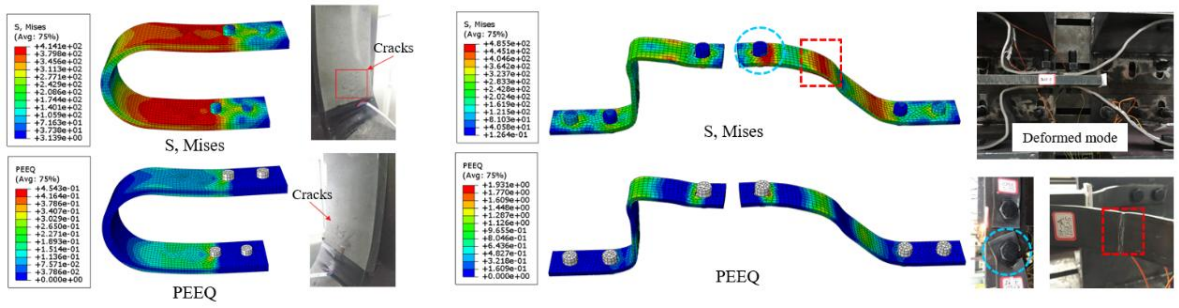

(a) USPD (b) SSPD

Figure 6. Plasticity distribution of numerical models and test specimens

4. Performance Evaluation under Cyclic Loading

4.1. Numerical Cases

A total of 24 numerical models are respectively established for USPD and SSPD to evaluate their seismic performance. Table 2 summarizes the models' dimensional parameters. Various plate widths, B, including 120 mm, 140 mm, 145 mm, 160 mm, 170 mm, 200 mm, and 250 mm are considered. Plate thicknesses, t, include 8 mm, 10 mm, 12 mm, and 14 mm. The radius, R, of 75 mm, 100 mm, and 125 mm is adopted. The length of the ending straight segment, L, for all cases is 200 mm, and the diameter of the bolts, d, is 18 mm. The material's Young's modulus of 206 GPa and yielding strength of 258 MPa, measured from the tensile coupon tests [29], are adopted during the model establishment.

Table 2. Dimensional parameters of the numerical models (unit: mm)

Model	*B*	*t*	*R*	*L*	*d*	Model	*B*	*t*	*R*	*L*	*d*
B250t8R75	250	8	75	200	18	B200t8R75	200	8	75	200	18
B250t8R100	250	8	100	200	18	B200t8R100	200	8	100	200	18
B250t8R125	250	8	125	200	18	B200t8R125	200	8	125	200	18
B200t10R75	200	10	75	200	18	B160t10R75	160	10	75	200	18
B200t10R100	200	10	100	200	18	B160t10R100	160	10	100	200	18
B200t10R125	200	10	125	200	18	B160t10R125	160	10	125	200	18
B170t12R75	170	12	75	200	18	B140t12R75	140	12	75	200	18
B170t12R100	170	12	100	200	18	B140t12R100	140	12	100	200	18
B170t12R125	170	12	125	200	18	B140t12R125	140	12	125	200	18
B145t14R75	145	14	75	200	18	B120t14R75	120	14	75	200	18
B145t14R100	145	14	100	200	18	B120t14R100	120	14	100	200	18
B145t14R125	145	14	125	200	18	B120t14R125	120	14	125	200	18

Displacement-controlled loading is employed when performing the analyses. Standard cyclic loading determined by the FEMA 461 protocol I [30] is exerted for assessing the hysteretic performance, the protocol of which is illustrated in Figure 7(a). The displacement amplitude of the first loading level is 1.04 mm, then it grows gradually with an increasing factor of 1.4 until the assumed maximum design displacement Δ_m=30 mm is attained. After that,

the amplitude increasement of $0.3\Delta_m$ is applied between the adjacent loading levels until the damper fails. Each loading level is repeated twice. In addition, the loading protocol suggested by T/CECS 900-2021 [31] is adopted to understand the performance of the dampers under low-cycle fatigue loading, as depicted in Figure 7(b). The loading criterion is on the basis of structural inter-story drift ratio (ISDR) response. It first requires three times-repeated loading cycles with an amplitude of elastic ISDR limitation. In this study, the limitation is adopted as 1/550. Subsequently, the loading ISDR amplitude increases to 1/150, 1/100, 1/75, 1/50, and 1/40 in sequence. Other than the last level, which is applied by one cycle, the rest are repeated three times. The low-cycle fatigue performance will be discussed in Section 5.

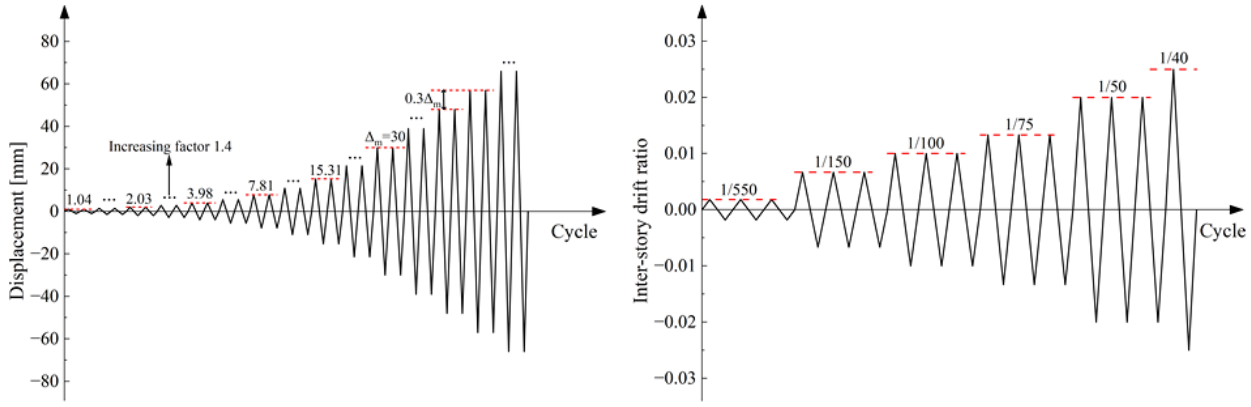

(a) Standard cyclic loading

(b) Low-cycle fatigue loading

Figure 7. Loading protocol

4.2. Hysteresis Characteristics

Figure 8 shows the comparison of hysteretic curves for some of the numerical models. It is found that the flexural deformation-dominated USPD exhibits bilinear hysteresis on the whole, while SSPD displays multi-stage hysteresis as the deformation mode switches between bending and tension. When the displacement load is at a relatively high level, the deformation mode of SSPD transfers to tension, inducing a secondary strengthening behavior with significantly increased post-yielding stiffness and load-bearing capacity. Accompanying with this behavior, a double stage of energy dissipation emerges and assists SSPD to achieve control of multi-level seismic responses. Also, obvious strength degradation for the second cycle of loading level at large displacement is observed for SSPD, owing to the squeezing deformation of the steel plate. This may cause adverse effects on the damper's fatigue performance. In addition, much higher initial stiffness, post-yielding stiffness, and peak strength can be easily discovered for SSPD, compared to USPD with identical geometric dimensions, due to the tension strengthening effect. For instance, the peak strength of SSPD models ranges from 400kN to 500kN, while that of USPD models is much lower than 100kN. In practical seismic design, it is expected that when suffering SLEs SSPD remains elastic to supply considerable stiffness and strength for displacement control. When it increases to DBE level, SSPD enters the first yielding stage to dissipate energy for damage control. And the second yielding stage of SSPD will be reached at MCE level, during which energy dissipation and large secondary stiffness from SSPD are beneficial for controlling damage and residual displacement.

To further compare the key mechanical parameters between USPD and SSPD models, a multi-linear model with four feature points is defined for describing mechanical characteristics of SSPD. It is separated into elastic, flexural yielding, tensile strengthening and failure segments by four feature points that are respectively the yielding point (F_y Δ_y), the strengthening point (F_t Δ_t), the peak point (F_p Δ_p), and the failure point (F_u Δ_u), as shown in Figure 9. The criteria for determining these points are the principles of tangent intersection and energy balance [29]. Specifically, the yielding point (F_y Δ_y) is defined as the intersection of tangent lines of elastic and flexural yielding segments. The peak point (F_p Δ_p) and Δ_u can be extracted from the backbone curve. The second yielding point (F_t Δ_t) is determined by two criteria: (a) a point on tangent lines of flexural yielding segment; (b) the area under multi-linear model before entering failure stage equals to the counterpart of backbone curve. Similarly, F_u is determined based on the principle of energy balance. Then stiffness k_1 and k_2 can be calculated. As the behavior of bilinear hysteresis, only the yielding and peak points are required for USPD. The determination of them is on the basis of tangent intersection principle.

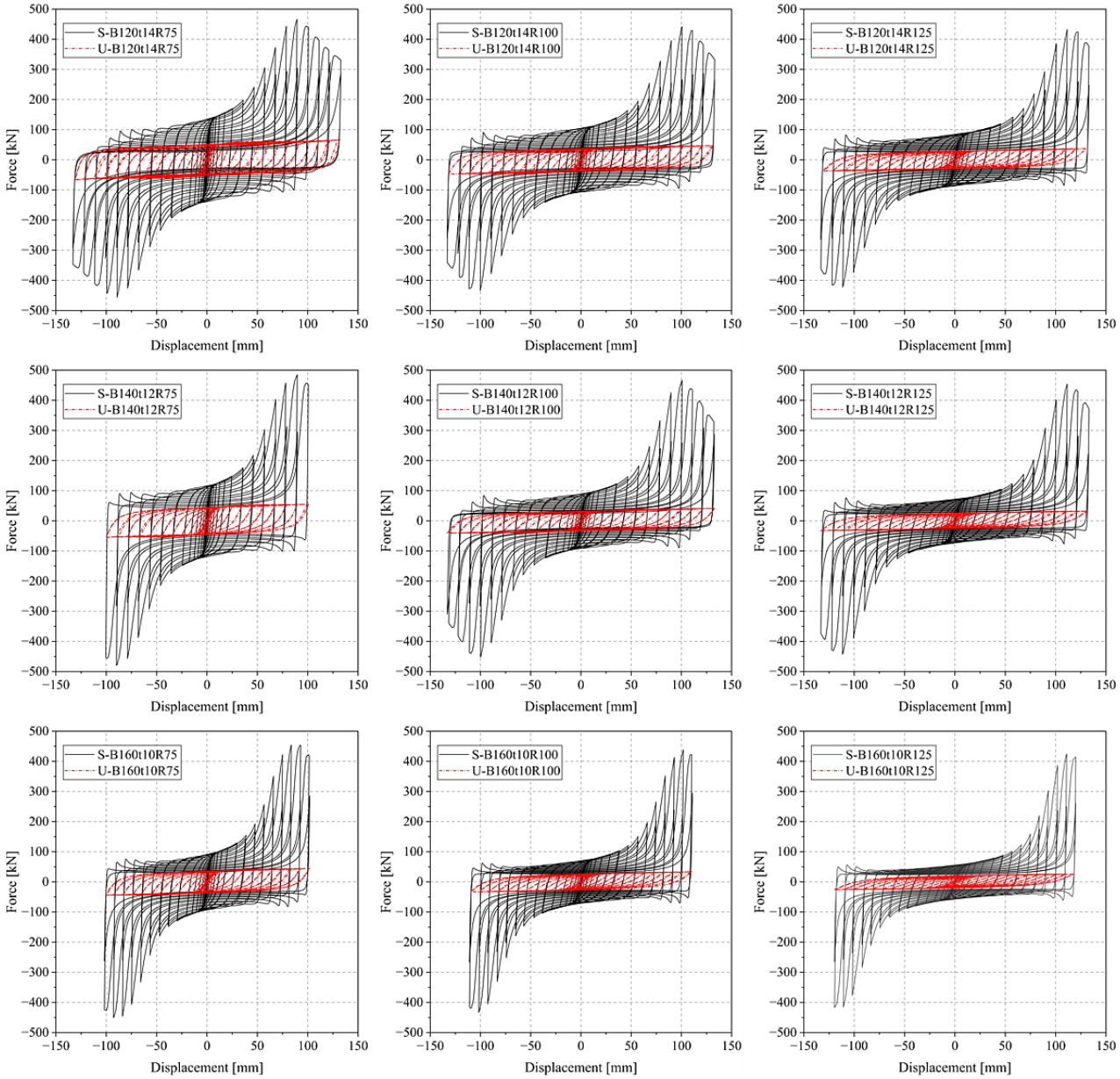

Figure 8. Comparison of hysteretic curves for the U- and S- models

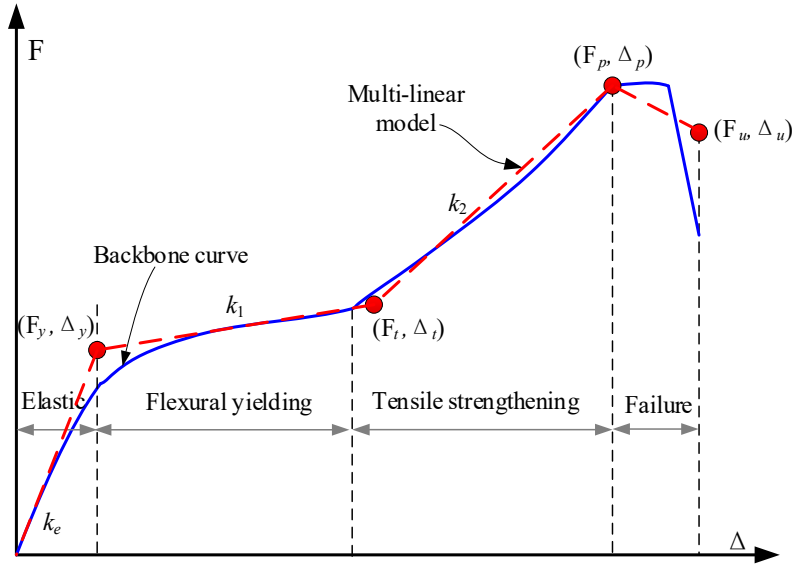

Figure 9. Definition of feature points [29]

Based on the above, the dampers' mechanical parameters can be obtained, as compared in Figure 10. The initial stiffnesses of SSPD $k_{e,S}$ are 6 ~ 8 times that of USPD $k_{e,U}$, and the ratio of $k_{e,S}$ to $k_{e,U}$ increases with the growth of R. The post yielding stiffnesses of SSPD $k_{1,S}$ are up to dozens of times that of USPD $k_{1,U}$, and the ratio of $k_{1,S}$ to $k_{1,U}$ decreases with the growth of R. Moreover, the strengthening stiffness $k_{2,S}$ of most SSPD models is much larger than $k_{e,U}$ of USPD, and their ratios $k_{2,S}/k_{e,U}$ range from 0.8 to 12. Figure 10(d), (e) and (f) respectively compare their yielding strengths, yielding displacements and peak strengths. It is found that the yielding displacement of SSPD is much lower than that of USPD, but the yielding strength is 2~3 times and the peak strength is 7 ~ 19 times those of USPD. As the increasement of R, the strength ratios $F_{y,S}$ / $F_{y,U}$ and $F_{p,S}$ / $F_{p,U}$ gradually increase. The analysis of stiffness and strength characteristics indicates that higher performance makes SSPD capable of providing large additional stiffness and strength to structures, thereby enhancing the structural seismic performance.

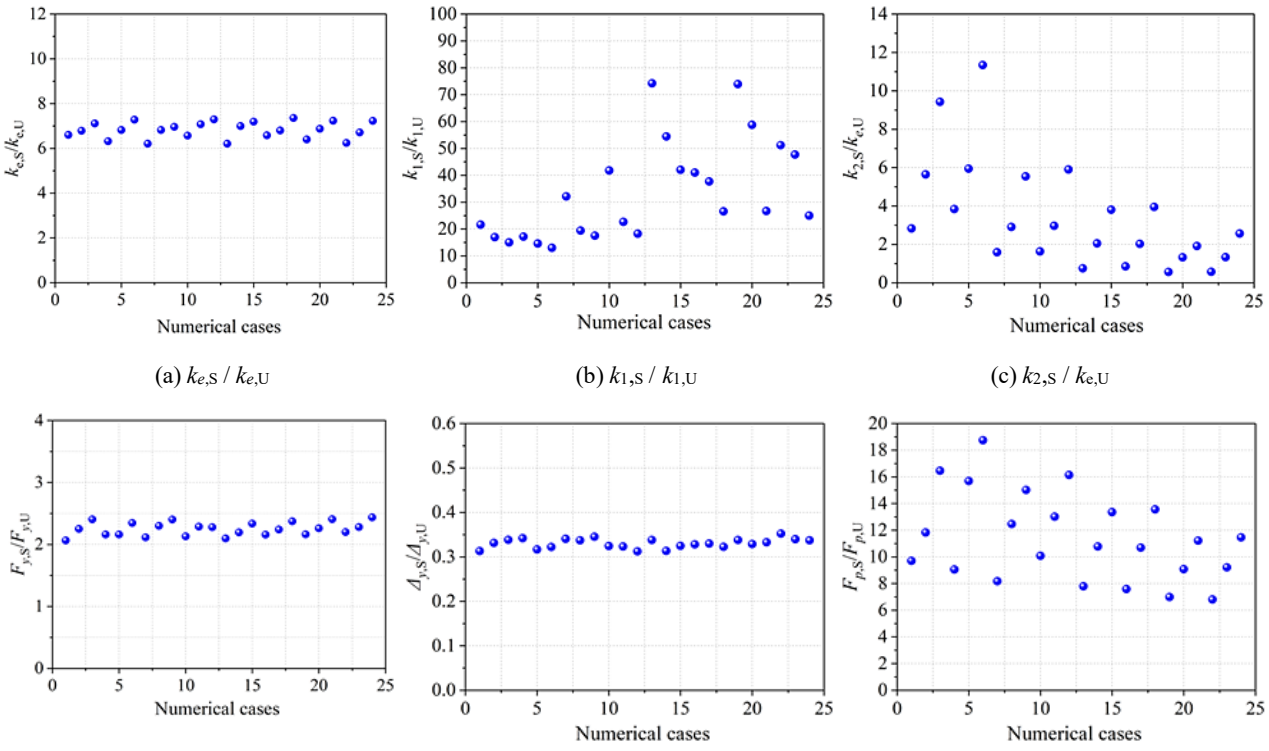

(a) $k_{e,S}$ / $k_{e,U}$ (b) $k_{1,S}$ / $k_{1,U}$ (c) $k_{2,S}$ / $k_{e,U}$

(d) $F_{y,S}$ / $F_{y,U}$ (e) $\Delta_{y,S}$ / $\Delta_{y,U}$ (f) $F_{p,S}$ / $F_{p,U}$

Figure 10. Comparison of mechanical parameters

4.3. Damage Development

Figure 11 takes the models U- and S-B145t14R75 as examples to compare the stress distribution at various loading steps. On the whole, the stress level of S-B145t14R75 is higher than that of the U-shaped counterpart, which is in harmony with the previous conclusion that SSPD has much higher bearing capacity. For U-B145t14R75, the high stress region is located at the junction of the straight segment and semi-circular arc segment. With the loading amplitude increases, this stress region extends towards the middle of the arc segment. For U-B145t14R75, a wider high stress region can be observed, and it not only locates at the junction of the straight segment and the arc segment, but also in the middle of the quarter-circular arc segment. Hence, it can be inferred that the damage and plastic development of SSPD is more extensive, reflecting its better material utilization rate. Figure 10 also demonstrates that the deformation mode of USPD does not vary with the increase of external load, while a noticeable mode change appears in SSPD at a relatively large load.

Figure 12 presents the PEEQ distribution of some models at the final stress state, from which a similar conclusion to the above can be obtained. For instance, the PEEQ of USPD models mainly concentrates on the junction region of the straight segment and semi-circular arc segment, and for SSPD, it mainly concentrates on the middle of the quarter-circular arc segment. The total area of the plastic region for SSPD is obviously larger than that of USPD, as well as the peak value of PEEQ, due to the rapid increase of stress in the tension strengthening stage. These observations are in accordance with the distribution rule of stress, demonstrating the SSPD's higher material utilization efficiency again.

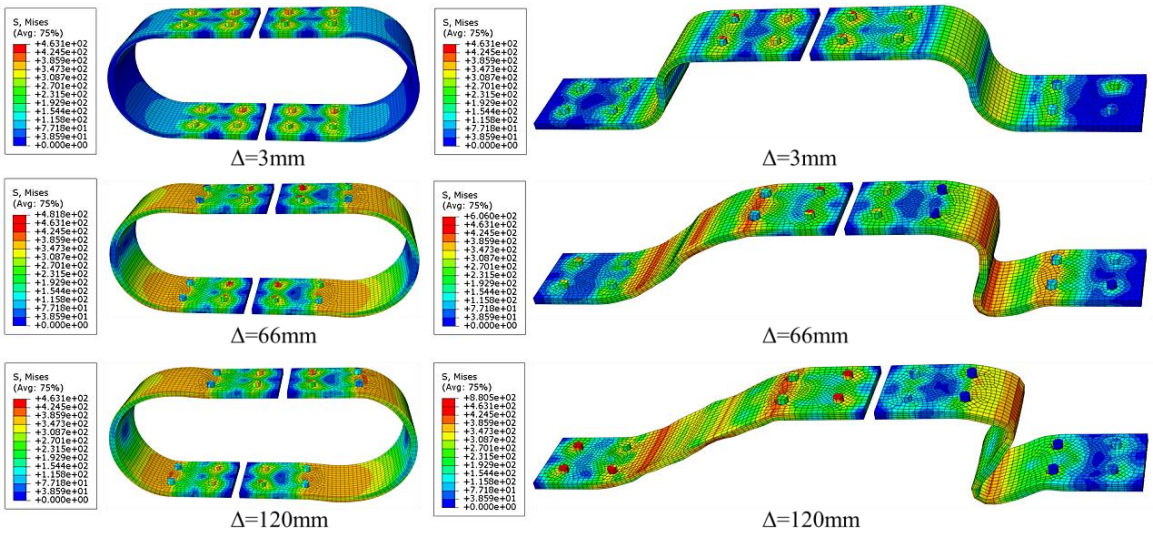

(a) USPD (b) SSPD

Figure 11. Stress distribution of models U- and S- B145t14R75

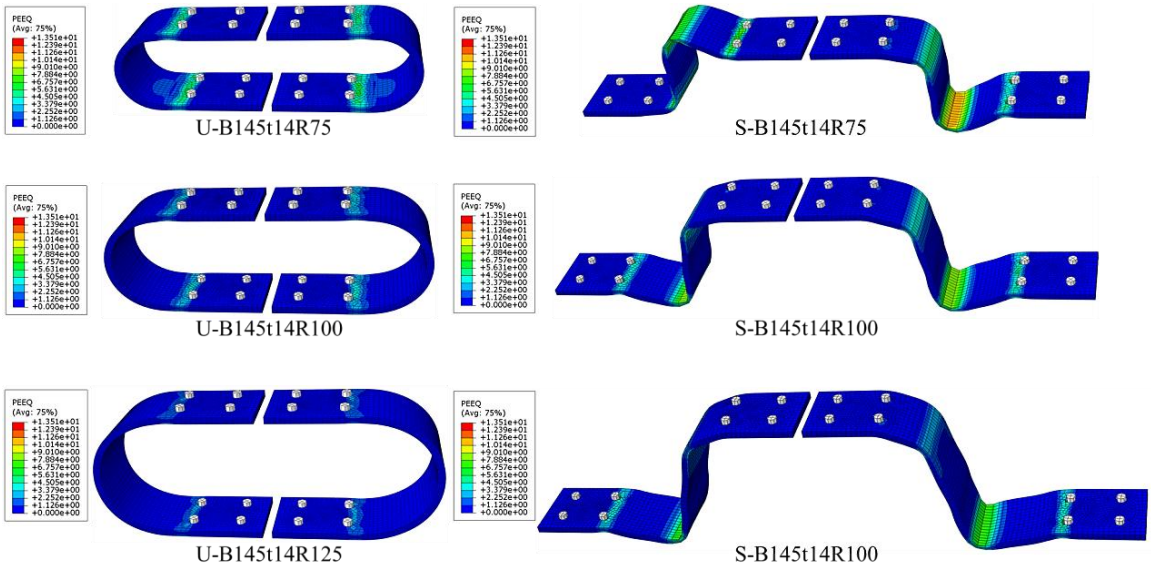

(a) USPD (b) SSPD

Figure 12. PEEQ distribution of the models

4.4. Stiffness Degradation

Stiffness degradation behavior can be generally described through equivalent stiffness as expressed by:

$$k_{eff} = \frac{|P_{\max}| + |P_{\min}|}{|\Delta_{\max}| + |\Delta_{\min}|} \tag{7}$$

where, k_{eff} is the equivalent stiffness at a given loading cycle; $P_{\max}$ and $P_{\min}$ are the maximum force at positive and negative loading directions, respectively; $\Delta_{\max}$ and $\Delta_{\min}$ are the displacements corresponding to $P_{\max}$ and $P_{\min}$. The obtained curves of equivalent stiffness versus displacement are plotted in Figure 13, by taking some of the models as examples. Overall, the degradation rules of equivalent stiffness, along with the loading displacement for USPD and SSPD, are not affected by the damper dimensions. Similar to other types of metallic dampers, the equivalent stiffness of USPD decreases quickly after the occurrence of yielding. For SSPD, it decreases like USPD at the flexural yielding stage, and then has a temporary ascending as a result of tensile strengthening. Additionally, the equivalent stiffness of SSPD is obviously higher than that of USPD during the whole loading process. Particularly, the equivalent stiffness of USPD under relatively large displacement approaches zero, while SSPD still exhibits a certain stiffness effect, which is beneficial for mitigating the structural displacement response and avoid structural collapse under strong earthquakes.

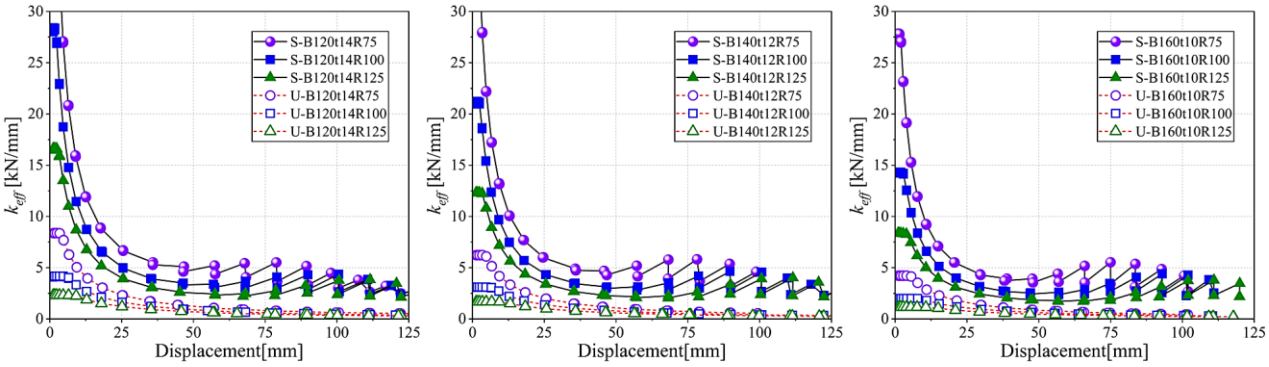

Figure 13. Stiffness degradation of some models

4.5. Energy Dissipation

Figure 14 depicts the variation curve of cumulative energy dissipation, taking some models as examples. For all models, the cumulative energy dissipation increases nonlinearly with the number of loading cycles, and the growth rate accelerates as the loading proceeds, which is attributed to the progressive plastic deformation and energy dissipation mechanism of the models. It is found that the model with lower parameter *R* dissipates more energy, for both USPD and SSPD, suggesting that the parameter *R* has a positive influence on the energy dissipation performance. Compared with USPD (with "U" prefix), SSPD (with "S" prefix) models dissipate energy earlier than USPD counterparts due to the smaller yielding displacement, and dissipate much more energy due to the higher bearing capacity. For instance, at 50 cycles, the cumulative energy dissipation of SSPD reaches up to 600 kJ, while that of the USPD is only about 300 kJ, indicating the superior energy dissipation capacity of SSPD. To quantitatively compare, Figure 15 illustrates the total energy dissipation of all the models. In most numerical cases, the total energy of SSPD model exceeds that of USPD model by a percentage larger than 200%, which means the former is more than three times the latter. The minimum and maximum exceedances are respectively 86% and 394%. It means that the energy dissipation capacity of SSPD is about 2~5 times that of USPD. Overall, the results demonstrate that the SSPD has a more excellent energy dissipation performance than the USPD, demonstrating the potential superiority employing SSPD for seismic mitigation of structures. And the parameter *R* plays a crucial role in enhancing the energy dissipation capacity of the dampers.

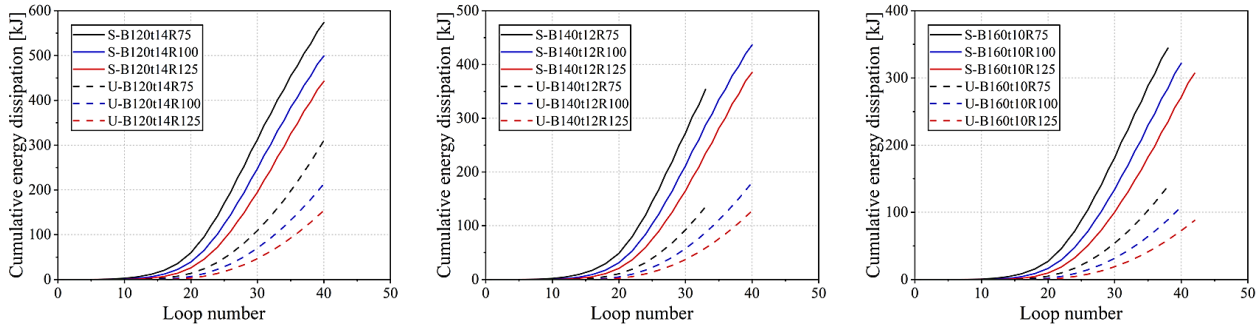

Figure 14. Cumulative energy dissipation of some models

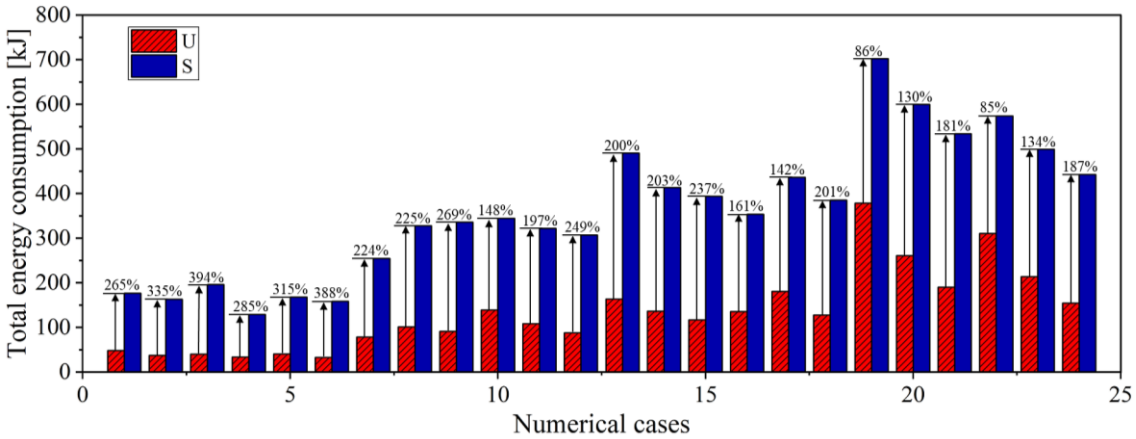

Figure 15. Total energy dissipation of the models

4.6. Residual Displacement

Residual displacement is an important indicator to assess the seismic resilience of structures. The damper with a larger residual displacement after being damaged will be more difficult to replace, and will inevitably deteriorate the structural seismic resilience. Therefore, Figure 16 compares the variation curve of residual displacement between the USPD and SSPD models. As the displacement load increases, the dampers' plastic deformation gradually develops, leading the increasement of the residual displacement. Because the plastic damages in the SSPD models is more severe, as mentioned in Section 4.3, their residual displacement is larger than that of USPD models. To quantitatively analyse the difference between them, Figure 17 lists the maximum residual displacement of all the models. As can be seen, the residual displacement of SSPD models is 2%~40% larger than that of USPD models, and the median value of the relative difference is about 12.5%. Moreover, there are 16 cases where the relative difference is less than 15% and 8 cases where the relative difference is less than 10%. These results indicate that although the residual displacement of SSPD is larger than that of USPD, it can be maintained at the same level by adjusting the dimension parameters of the damper.

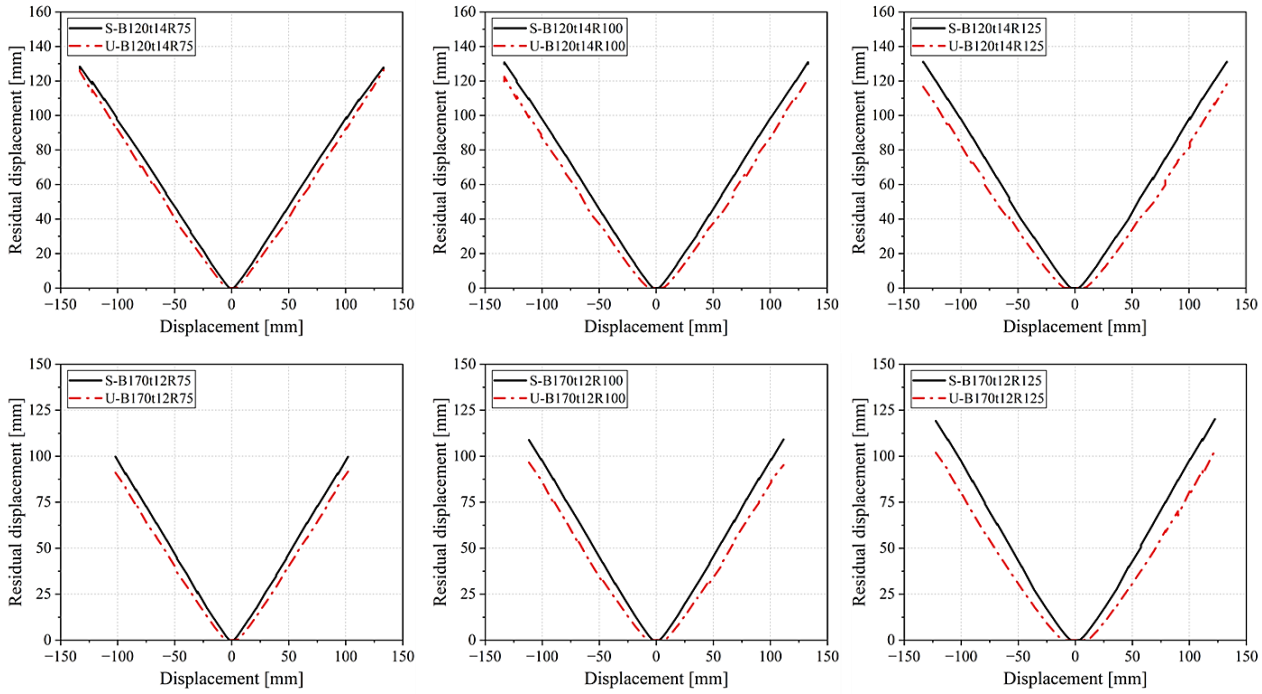

Figure 16. Residual displacement of some models

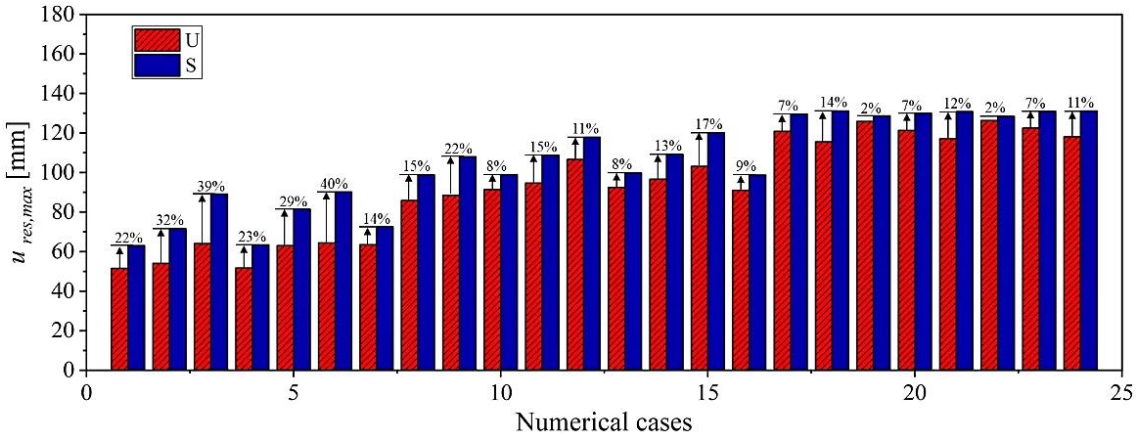

Figure 17. The maximum residual displacement of the models

5. Performance Evaluation under Low-cycle Fatigue Loading

According to the loading protocol shown in Figure 6(b), low-cycle fatigue loading can be applied to the models by assuming the structural height to be 3 m. Here, a total of six models with dimensions of B200t8R100, B160t10R100 and B200t10R100 are analyzed for USPD and SSPD. Figure 18 compares their low-cycle fatigue hysteretic curves. There is no degradation in stiffness and strength observed during the repeated loading cycles for USPD models, while obvious stiffness and strength degradations occurred in SSPD models when the dampers enter to secondary strengthening stage.

From this perspective, it can be assumed that the low-cycle fatigue performance of SSPD under large displacement is inferior to that of USPD, since the standard JGJ 297 [32] have imposed strict limitations on the degree of degradation. Nonetheless, the descending segment of the skeleton curve does not appear in SSPD models, indicating that the models have not failed under the applied fatigue loading protocol. Figure 19 shows the final PEEQ distribution of the models, from which a similar phenomenon to Figure 12 can be observed. The developmental plasticity of the SSPD models is much more severe than that of the USPD models, revealing that the SSPD models have a higher capacity for cumulative plastic deformation. More importantly, the indicator of cumulative plastic deformation is critical to quantitatively evaluate the low-cycle fatigue performance [31, 33].

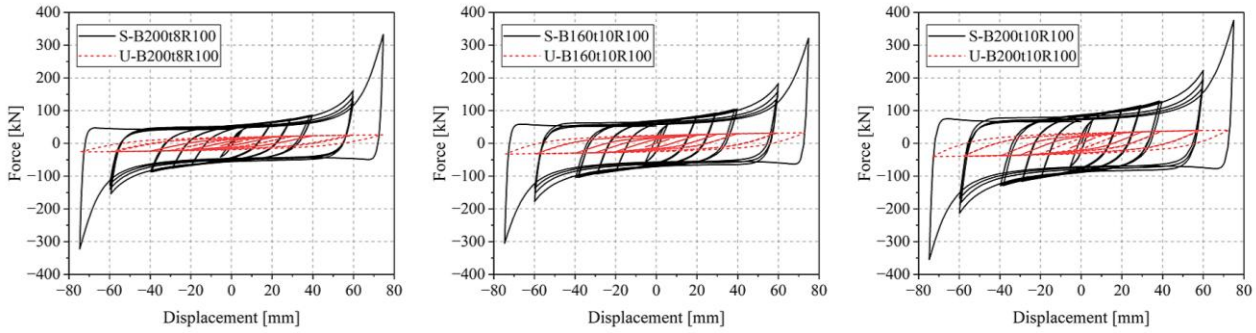

Figure 18. Hysteretic curves under low-cycle fatigue loading

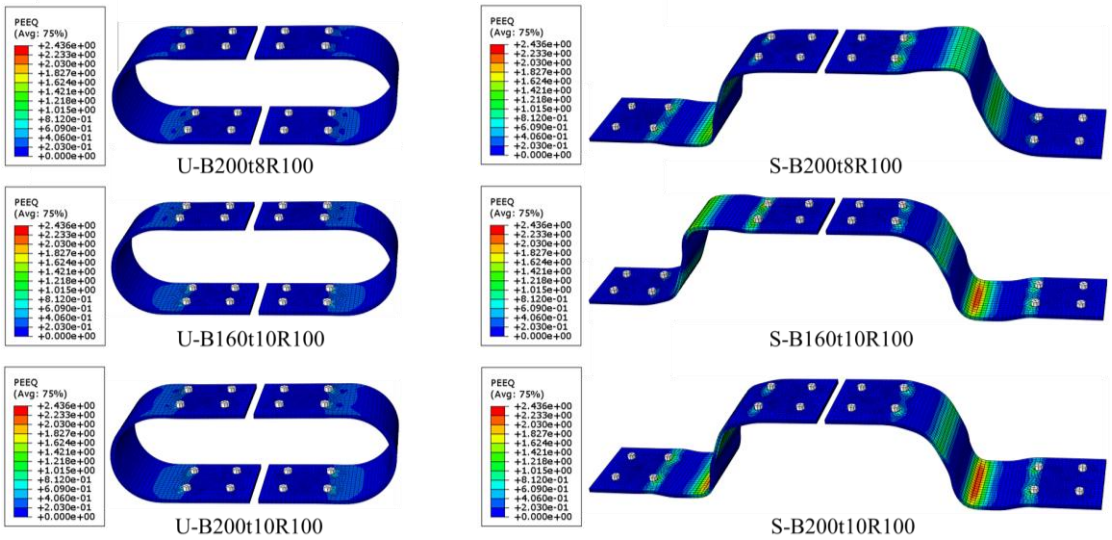

Figure 19. PEEQ distributions under low-cycle fatigue loading

In the codes T/CECS 900-2021 [31] and ANSI/AISC-341-16 [33], the cumulative plastic ductility (CPD) is employed for the performance evaluation under low-cycle fatigue loading, which can be obtained by:

$$\mu_{\mathrm{CPD}} = \sum \left[\frac{2\left(\left|\Delta_i^+\right| + \left|\Delta_i^-\right|\right)}{\Delta_y} - 4 \right] \tag{8}$$

where, μ_{CPD} is the cumulative plastic ductility; Δ_y is the yielding displacement; Δ_i^+ and Δ_i^- are the positive and negative maximum displacement at the ith loading cycle, respectively. The calculated μ_{CPD} for each model is provided in Figure 20. The values of μ_{CPD} for SSPD models are 313.12, 371.80 and 367.00, respectively, while those of the USPD counterparts are 101.37, 113.68 and 119.45. The former exceeds the latter by more than three times. In code T/CECS 900-2021 [31], a lowest limitation of 351.6 is specified for μ_{CPD} when using steel material Q235 to manufacture loading-bearing and energy-dissipating components. Accordingly, it can be found that the low-cycle fatigue performance of SSPD models basically meets the code requirement, but for the USPD models the μ_{CPD} is far from meeting the lowest limitation. Even using the lowest limitation of 200 specified in code ANSI/AISC-341-16 [33], the results of the USPD models are still unable to meet the requirement. Overall, across all the models, SSPD exhibits significantly higher CPD with the ductility values being about 3 to 3.3 times those of USPD. This indicates that SSPD has a stronger plastic deformation capacity, which are attributed to their two-stage yielding behavior. And it can be deduced that the low-cycle fatigue performance of SSPD is far superior to that of USPD on the perspective of CPD.

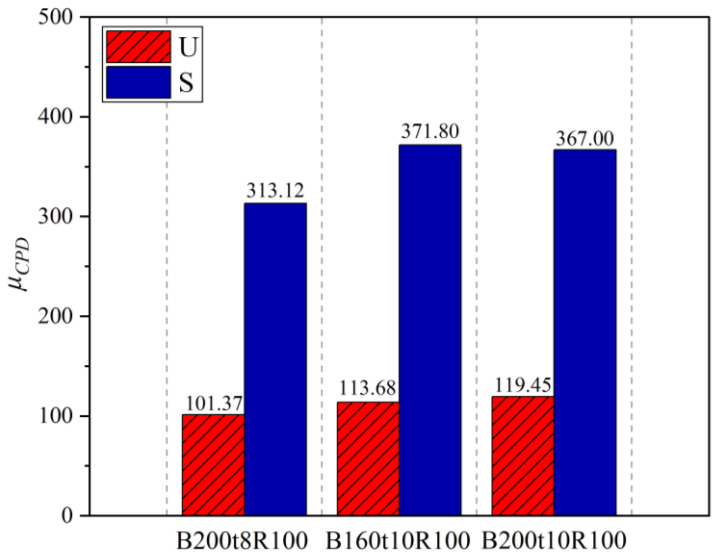

Figure 20. Cumulative plastic ductility of the models

6. Design Formulas for Engineering Practice

In Section 2, the theoretical formulas for calculating initial stiffness and yielding strength of USPD and SSPD are provided, but they fail to completely describe the dampers' skeleton curves, and would not be applicable in actuality owing to the ideal boundary assumption. To facilitate the application in engineering practice, design formulas will be obtained in the following by data fitting of the numerical results. Although a previous study has provided practical design equations for predicting the key mechanical properties of SSPD, they were obtained by fitting the numerical data under ideal fixed boundary conditions. And this study is more in line with actual boundary conditions and has greater generality.

As illustrated in Figure 9, a total of four feature points are needed for determining the skeleton curve of SSPD, including the yielding point, the strengthening point, the peak point, and the failure point. Firstly, the relationships between nominalized yielding displacement, initial stiffness and the geometric dimensions are fitted to determine the yielding point, as plotted in Figures 21(a) and 21(b). The nominalized yielding displacement Δ_y / ($\sigma_y t$ / E) increases nonlinearly with the parameter $2R/t$, following the equation $y = 3.19x^{1.60}$ with R-Square = 0.98, while the nominalized initial stiffness k_e / (EB) decreases nonlinearly with the parameter $2R/t$, following the equation $y = 0.89x^{-2.54}$ with R-Square = 0.99. Thus, the formulas for yielding displacement and initial stiffness can be inverted as:

$$\Delta_{y,\mathrm{S}} = 3.19\frac{\sigma_y t}{E}\left(\frac{2R}{t}\right)^{1.60} \tag{9}$$

$$k_{e,\mathrm{S}} = 0.89EB\left(\frac{2R}{t}\right)^{-2.54} \tag{10}$$

where, Δ_y is the yielding displacement and the subscript 'S' represents SSPD; other parameters are the same as mentioned in Section 2. Then, the fitting relationships for Δ_p / Δ_y and F_p are obtained to determine the peak point, as shown in Figure 21(c) and 21(d). It can be seen that Δ_p / Δ_y decreases nonlinearly with the parameter ($2R/t$ + 1), following the equation $y = 428.24x^{-1.01}$ with R-Square = 0.94, while F_p increases linearly with the parameter $\sigma_y Bt$, following the equation $y = 0.996x$ with R-Square = 0.99. Accordingly, the corresponding formulas are expressed by Equations 11 and 12, where Δ_p and F_p are the peak displacement and force, respectively.

$$\Delta_{p,\mathrm{S}} = 428.24\Delta_y\left(\frac{2R}{t}+1\right)^{-1.01} \tag{11}$$

$$F_{p,\mathrm{S}} = 0.996\sigma_y Bt \tag{12}$$

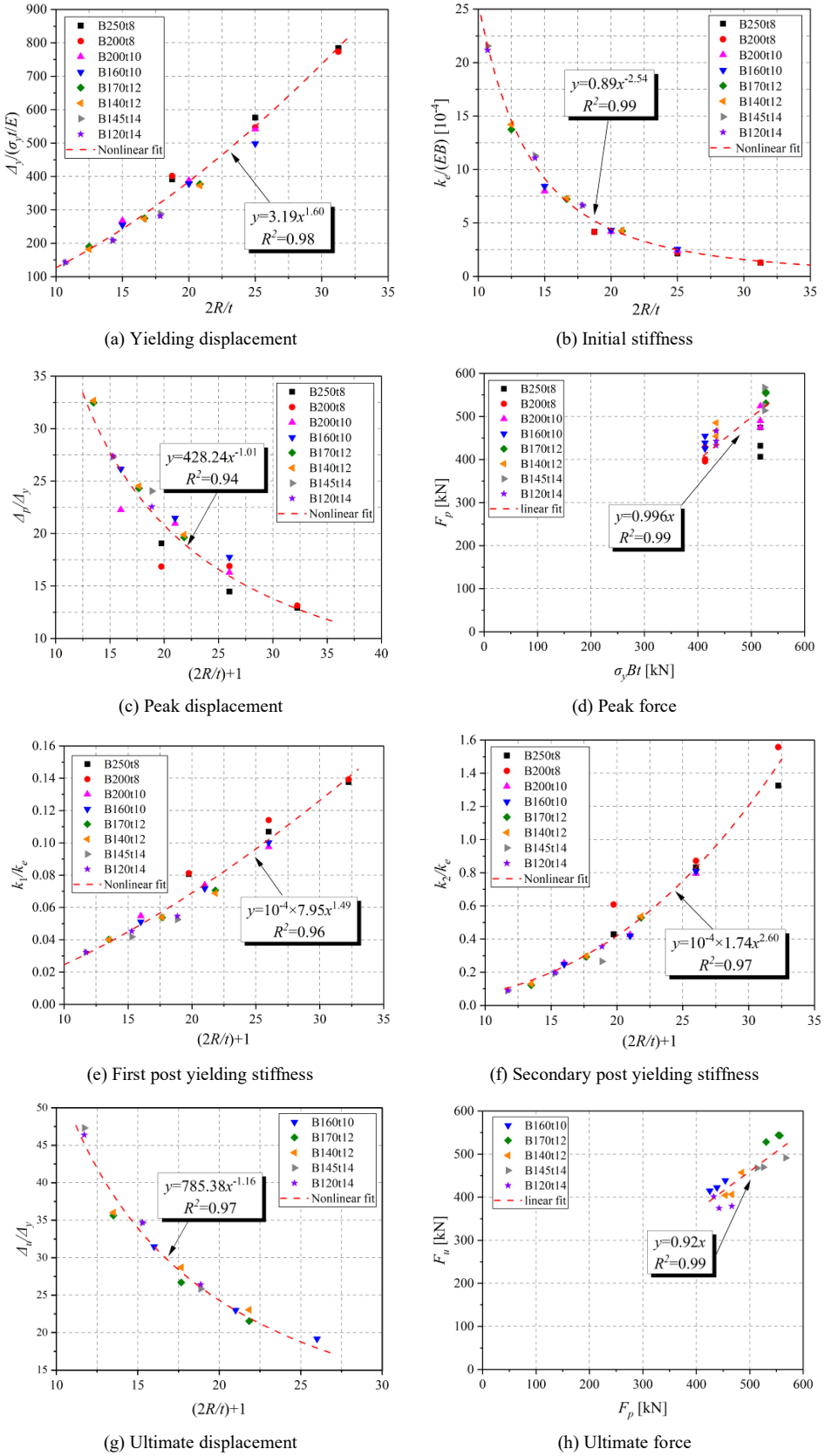

Figure 21. Design formula fitting for SSPD

Thirdly, the first and secondary post yielding stiffness ratios k_1 / k_e, k_2 / k_e are fitted as Figures 21(e) and 21(f). k_1 / k_e increases nonlinearly with the parameter $(2R/t + 1)$, following the equation $y = 10^{-4}\times7.95x^{1.49}$ with R-Square = 0.96, while k_2 / k_e increases nonlinearly with the parameter $(2R/t + 1)$, following the equation $y = 10^{-4}\times1.74x^{2.60}$ with R-Square = 0.97. Furthermore, the first and secondary post yielding stiffness can be obtained as Equations 13 and 14. By combining them with the yielding and peak points, the strengthening point can be determined.

$$k_{1,S} = 7.95\times10^{-4} k_e \left(\frac{2R}{t}+1\right)^{1.49} \tag{13}$$

$$k_{2,S} = 1.74\times10^{-4} k_e \left(\frac{2R}{t}+1\right)^{2.60} \tag{14}$$

Finally, Figures 21(g) and 21(h) gives the fitting relationships for Δ_u/Δ_y and F_u. As it can be seen, Δ_u / Δ_y decreases nonlinearly with the parameter $(2R/t + 1)$, following the equation $y = 785.38x^{-1.16}$ with R-Square = 0.97, while F_u increases linearly with the parameter F_p, following the equation $y = 0.92x$ with R-Square = 0.99, following which the ultimate displacement and capacity can be respectively calculated by Equations 15 and 16 to determine the failure point.

$$\Delta_{u,S} = 785.38\Delta_y \left(\frac{2R}{t}+1\right)^{-1.16} \tag{15}$$

$$F_{u,S} = 0.92F_p \tag{16}$$

Considering that the hysteretic behavior of USPD can be idealized by a bilinear skeleton model, three mechanical parameters, including initial stiffness $k_{e,U}$, yielding displacement $\Delta_{y,U}$ and post-yielding stiffness $k_{1,U}$, are enough for its design. Figures 22(a) and 22(b) plot the fitting relationships between the nominalized initial stiffness, yielding displacement and the geometric parameters, based on which $k_{e,U}$ and $\Delta_{y,U}$ can be obtained as Equations 17 and 18. Figure 22(c) gives the relationship between $k_{1,U} / k_{e,U}$ and the geometric parameters, from which the post-yielding stiffness can be calculated by Equation 19.

$$k_{e,U} = 0.21EB\left(\frac{2R}{t}\right)^{-2.70} \tag{17}$$

$$\Delta_{y,U} = 9.52\frac{\sigma_y t}{E}\left(\frac{2R}{t}\right)^{1.60} \tag{18}$$

$$k_{1,U} = 4.17\times10^{-6} k_e \left(\frac{2R}{t}+1\right)^{2.78} \tag{19}$$

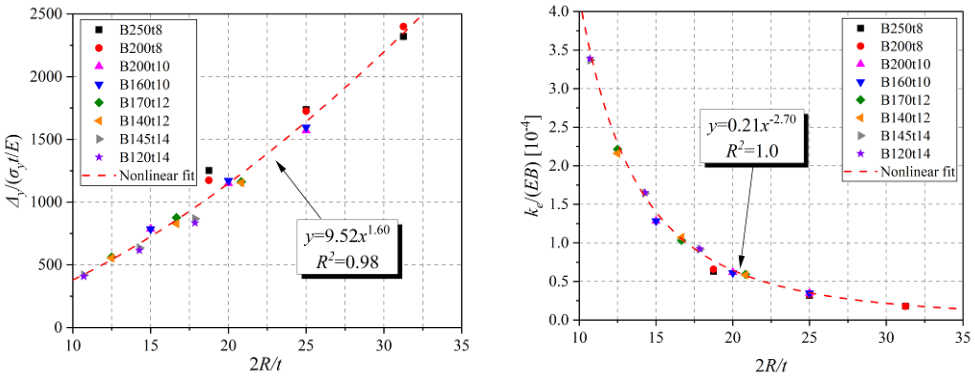

(a) Yielding displacement

(b) Initial stiffness

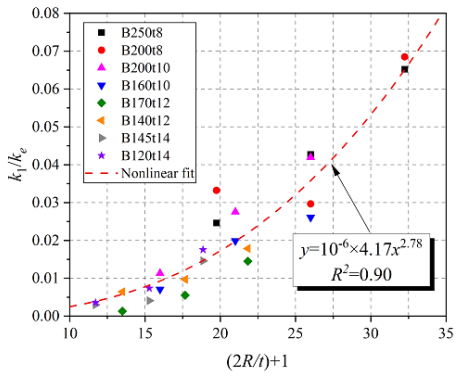

(c) Post yielding stiffness

Figure 22. Design formula fitting for USPD

7. Conclusion

This study proposes a new steel damper, the SSPD, derived from the USPD, and conducts a comparative investigation into their cyclic behaviors through validated numerical simulations and parametric analyses, with a focus on hysteretic performance, low-cycle fatigue resistance and design formulas of engineering application. The SSPD demonstrates distinct advantages over the USPD in seismic mitigation. It adopts a flexural-tensile deformation mode, enabling double-stage energy dissipation for multi-level seismic response control, whereas the USPD relies on a single yielding stage. When geometric dimensions are identical, the SSPD exhibits markedly superior mechanical properties: its initial stiffness is 6 ~ 8 times, yielding strength is 2 ~ 3 times, and peak strength is 7 ~ 19 times those of the USPD, providing structures with enhanced stiffness and strength against seismic loads. Additionally, the SSPD's energy dissipation capacity is 2 ~ 5 times greater than the USPD's, with only a 12.5% median increase in residual displacement, indicating its potential for effective seismic mitigation. Under low-cycle fatigue loading, the values of μ_{CPD} for SSPD models are 313.12, 371.80, and 367.00, respectively, while those of the USPD counterparts are 101.37, 113.68, and 119.45. The CPD of USPD is much lower than that of SSPD and is far from meeting the code requirement. In contrast, SSPD is capable of meeting the requirement, indicating the superior fatigue performance of SSPD. Finally, the fitting design formulas for both dampers show good correlation and are applicable in engineering practice. Leveraging its enhanced mechanical properties, energy dissipation, and fatigue resistance, the proposed SSPD can function as a dual-purpose component for load-bearing and energy dissipation in real-world applications.

It is worth noting that the practical design scenarios often involve independent optimization of damper shapes based on constraints such as equal material weight or equal initial stiffness, which may influence the performance comparison between SSPD and USPD. When both dampers are optimized to have the same material weight, SSPD may not outperform USPD because their mechanical performances are determined by several geometric parameters including height, thickness and width. If these parameters are identical, the performance of SSPD is better as illustrated in this study. However, when SSPD has higher height and lower thickness and width, its performance may be inferior. Under the constraint of equal initial stiffness, SSPD is like to outperform USPD because the double-stage energy dissipation mechanism enables SSPD dissipates more energy and provides significant secondary stiffness.

8. Declarations

8.1. Author Contributions

Conceptualization, Z.Z. and Y.H.; methodology, Z.Z. and Q.S.; software, Z.Z., Q.S., and K.Y.; validation, Q.S. and K.Y.; formal analysis, Q.S. and K.Y.; investigation, Z.Z. and Q.S.; resources, Z.Z. and Y.H.; data curation, Q.S. and L.W.; writing—original draft preparation, Z.Z. and Q.S.; writing—review and editing, Z.Z., Y.H., and L.W.; visualization, Q.S. and K.Y.; supervision, Y.H.; project administration, L.W.; funding acquisition, Z.Z. and Y.H. All authors have read and agreed to the published version of the manuscript.

8.2. Data Availability Statement

The data presented in this study are available in the article.

8.3. Funding and Acknowledgments

The authors would like to express their gratitude for the support received from various sources, including the National Natural Science Foundation of China (No.52308309), Young Talent Support Project of Guangzhou Association for Science and Technology (QT-2025-007), Special Subject on Basic and Applied Basic Research in Guangzhou City (2025A04J1486), Guangzhou City-University-Enterprise Joint Funding Project (2025A03J0067), and the Guangdong Basic and Applied Basic Research Foundation (No.2022A1515110191; 2023A1515011914).

8.4. Conflicts of Interest

The authors declare no conflict of interest.

9. References

[1] Ghabussi, A., Asgari Marnani, J., & Rohanimanesh, M. S. (2020). Improving seismic performance of portal frame structures with steel curved dampers. Structures, 24, 27–40. doi:10.1016/j.istruc.2019.12.025.

[2] Hashemi, B. H., & Alirezaei, M. (2018). On the Evaluation of the Use of EKBs to Improve Seismic Performance of Steel Frames. International Journal of Steel Structures, 18(1), 25–37. doi:10.1007/s13296-018-0303-8.

[3] Zhai, Z., Guo, W., Li, Y., Yu, Z., Cao, H., & Bu, D. (2019). An improved performance-based plastic design method for seismic resilient fused high-rise buildings. Engineering Structures, 199, 109650. doi:10.1016/j.engstruct.2019.109650.

[4] Park, M. J., Ghamari, A., & Jaya, R. P. (2025). An experimental and numerical study of an innovative flexural damper to improve the behavior of CBF braces. Structures, 76, 108935. doi:10.1016/j.istruc.2025.108935.

[5] Wang, W., Chen, S., Chen, B., Liu, G., Hua, X., & Chen, Z. (2025). Development and application of metallic dampers in bridge engineering: A review. Journal of Traffic and Transportation Engineering, 12(2), 236–268. doi:10.1016/j.jtte.2024.12.002.

[6] Zhang, H., Ke, K., Zhou, X., Yam, M. C. H., Wang, J., & Lin, Y. (2025). Multi-stage hybrid damper: Experimental validation and application in monopile offshore wind turbines. Ocean Engineering, 338, 121844. doi:10.1016/j.oceaneng.2025.121844.

[7] Zhai, Z., Li, S., Liu, Y., Ma, Y., Zou, S., & Zhou, F. (2022). Seismic retrofitting of SMRFs using varied yielding cross-section damper: A companion paper. Journal of Constructional Steel Research, 194, 107290. doi:10.1016/j.jcsr.2022.107290.

[8] Huang, W., Liu, G., Zhang, H., An, Y., & Fan, Z. (2025). Study on a novel type of metallic damper. Journal of Building Engineering, 101, 111854. doi:10.1016/j.jobe.2025.111854.

[9] Zheng, G., & Han, J. (n.d.). Seismic Performance of an Axial Compression-Tension, U-Shaped, and Thick-Walled Metal Bellows Damper. China Earthquake Engineering Journal, 46(6), 1318–1330. doi:10.20000/j.1000-0844.20230116003.

[10] Kato, S., & Kim, Y. B. (2006). A finite element parametric study on the mechanical properties of J-shaped steel hysteresis devices. Journal of Constructional Steel Research, 62(8), 802–811. doi:10.1016/j.jcsr.2005.11.014.

[11] Chong, X., Sha, H., Xie, L., Li, A., Jiang, Q., He, Y., & Chen, X. (2022). Experimental and Numerical Studies on the Seismic Performance of Precast Concrete Shear Wall Structures with an Energy Dissipation Cladding Panel. Journal of Earthquake Engineering, 26(6), 3264–3279. doi:10.1080/13632469.2020.1796843.

[12] Ebadi Jamkhaneh, M., Ebrahimi, A. H., & Shokri Amiri, M. (2019). Experimental and Numerical Investigation of Steel Moment Resisting Frame with U-Shaped Metallic Yielding Damper. International Journal of Steel Structures, 19(3), 806–818. doi:10.1007/s13296-018-0166-z.

[13] Taiyari, F., Mazzolani, F. M., & Bagheri, S. (2019). A proposal for energy dissipative braces with U-shaped steel strips. Journal of Constructional Steel Research, 154, 110–122. doi:10.1016/j.jcsr.2018.11.031.

[14] Qu, B., Dai, C., Qiu, J., Hou, H., & Qiu, C. (2019). Testing of seismic dampers with replaceable U-shaped steel plates. Engineering Structures, 179, 625–639. doi:10.1016/j.engstruct.2018.11.016.

[15] Liu, Y., Zhang, S., Hou, H., Qu, B., Song, W., Wang, J., & Zhou, Z. (2025). Seismic dampers with stacked thin U-shaped steel plates: Cyclic tests and numerical simulations. Structures, 79, 109572. doi:10.1016/j.istruc.2025.109572.

[16] Oh, S. H., Song, S. H., Lee, S. H., & Kim, H. J. (2013). Experimental study of seismic performance of base-isolated frames with U-shaped hysteretic energy-dissipating devices. Engineering Structures, 56, 2014–2027. doi:10.1016/j.engstruct.2013.08.011.

[17] Hui, Y. X., Li, L. S., Cheng, H., Zhang, Y. J., & Wang, D. S. (2023). Seismic mitigation of continuous girder bridges equipped with U-shaped stainless steel dampers under near-fault earthquake excitations. Structures, 58, 105597. doi:10.1016/j.istruc.2023.105597.

[18] Deng, K., Liang, H., Yi, Y., Zhao, C., Dai, S., & Wu, D. (2023). Sliding U-shaped steel damper for multi-directional displacement. International Journal of Non-Linear Mechanics, 156, 104483. doi:10.1016/j.ijnonlinmec.2023.104483.

[19] Xie, X., Chen, S. X., & Zhou, X. (2018). A simplified analytical model for U-shaped steel dampers considering horizontal bidirectional deformation. Bulletin of Earthquake Engineering, 16(12), 6243–6268. doi:10.1007/s10518-018-0407-8.

[20] Hu, X., Dong, H., Su, C., Han, Q., & Du, X. (2024). Experimental and numerical studies on hysteresis performance of U-shaped SMA-steel plates damper. Journal of Constructional Steel Research, 219, 108802. doi:10.1016/j.jcsr.2024.108802.

[21] Wang, B., & Zhu, S. (2018). Superelastic SMA U-shaped dampers with self-centering functions. Smart Materials and Structures, 27(5), 55003. doi:10.1088/1361-665X/aab52d.

[22] Zhai, Z., Liu, Y., Mercan, O., Zou, S., & Zhou, F. (2024). A hybrid buckling-restrained brace for enhancing the seismic performance of steel moment resisting frames. Soil Dynamics and Earthquake Engineering, 178, 108464. doi:10.1016/j.soildyn.2024.108464.

[23] Dai, K., Sun, T., Liu, Y., Li, T., & Camara, A. (2023). Concept and numerical analysis of a double-stage coupling damper for multilevel seismic protection. Thin-Walled Structures, 185, 110581. doi:10.1016/j.tws.2023.110581.

[24] Yang, C., Xie, L., Sun, H., Ban, H., Liu, B., & Li, A. (2025). Theoretical, experimental, and numerical investigations on friction-metallic hybrid asynchronized-type double-stage shear damper. Thin-Walled Structures, 211, 113107. doi:10.1016/j.tws.2025.113107.

[25] Wen, Q., Xie, L., Zhu, L., Yang, C., & Wang, X. (2025). Comparison of seismic resilience of steel frame structure equipped with double-stage and conventional buckling-restrained braces. Journal of Constructional Steel Research, 228, 109430. doi:10.1016/j.jcsr.2025.109430.

[26] Eghlimi, M., Memarzadeh, P., Abadi, E. I. Z., & Javadi, P. (2024). An innovative two-level yielding knee-braced frame with deformation-controlled ring damper. Case Studies in Construction Materials, 21, 3856. doi:10.1016/j.cscm.2024.e03856.

[27] Chen, Y., Chen, C., Jiang, H., Liu, T., & Wan, Z. (2019). Study of an innovative graded yield metal damper. Journal of Constructional Steel Research, 160, 240–254. doi:10.1016/j.jcsr.2019.05.028.

[28] Cheraghi, K., & TahamouliRoudsari, M. (2025). Parametric study of the innovative model of angled U-shape damper with multiphase yielding mechanism. International Journal of Non-Linear Mechanics, 170, 104998. doi:10.1016/j.ijnonlinmec.2024.104998.

[29] Zhai, Z., Guo, W., Yu, Z., He, C., & Zeng, Z. (2020). Experimental and numerical study of S-shaped steel plate damper for seismic resilient application. Engineering Structures, 221, 111006. doi:10.1016/j.engstruct.2020.111006.

[30] FEMA. (2007). Interim testing protocols for determining the seismic performance characteristics of structural and nonstructural components (FEMA 461). Applied Technology Council, California, United States.

[31] T/CECS 900-2021. (2022). Technical specification for seismic mitigation of loading-bearing and energy-dissipating. China Engineering Construction Standardization Association Standards, Beijing, China.

[32] JGJ 297. (2013). Technical specification for seismic energy dissipation of buildings (JGJ 297). Ministry of Housing and Urban-Rural Development of the People's Republic of China, China Building Industry Press, Beijing, China.

[33] ANSI/AISC 341-16. (2016). Seismic provisions for structural steel buildings. American Institute of Steel Construction, Chicago, United States.